Hydrometallurgy 198 (2020) 105514

Contents lists available at ScienceDirect

Hydrometallurgy

journal homepage: www.elsevier.com/locate/hydromet

In-situ reduction of $Au(S_2O_3)_2^{3-}$ for efficient recovery of gold with magnetically separable shell-core structured $MoS_2@Fe_3O_4$ composite

Kaige Sun [a], Shangjian Mao [a], Weiquan Zhan [a], Chang Liu [a], Feifei Jia [a,b,*], Shaoxian Song [a,b]

[a] Hubei Key Laboratory of Mineral Resources Processing and Environment, Wuhan University of Technology, Luoshi Road 122, Wuhan, Hubei 430070, China
[b] School of Resources and Environmental Engineering, Wuhan University of Technology, Luoshi Road 122, Wuhan, Hubei 430070, China

ARTICLE INFO

Keywords:
In-situ reduction
$Au(S_2O_3)_2^{3-}$
Magnetic separation
Heterostructure

ABSTRACT

Magnetic MoS_2 could be easily separated from water or solid suspensions. In this work, shell-core structured $MoS_2@Fe_3O_4$ composite was fabricated through hydrothermal method and used as catalyst for recovering gold-thiosulfate complex ions ($Au(S_2O_3)_2^{3-}$) in aqueous solution. The results suggested that $MoS_2@Fe_3O_4$ composite could effectively in-situ reduce $Au(S_2O_3)_2^{3-}$ to gold particles (Au^0) with an extremely high reduction capacity of 1541.1 mg/g; moreover, the gold loaded $MoS_2@Fe_3O_4$ could be easily collected using a magnetic separator. The mechanism of reducing $Au(S_2O_3)_2^{3-}$ to Au^0 was ascribed to the photoexcited electrons from $MoS_2@Fe_3O_4$ composite. More importantly, the incorporation of Fe_3O_4 could effectively enhance the transferred efficiency of photoexcited electrons and accelerate separation of electrons-holes pairs. With great gold reduction capacity and magnetic recyclability, the $MoS_2@Fe_3O_4$ composite could be a promising material for recovering gold from leaching solutions.

1. Introduction

Over the decades, cyanidation has been the predominant technique for extracting gold from ores (Sun et al., 2018a, 2018b). However, the highly toxic cyanide caused severe environmental problems. Thiosulfate leaching has received wide attention and is regarded as the most promising and eco-friendly substitution to cyanidation (Muir and Aylmore, 2004). The mechanism of thiosulfate leaching is expressed as the following equations (Liu et al., 2020):

$$Au + 5S_2O_3^{2-} + Cu(NH_3)_4^{2+} \rightarrow Au(S_2O_3)_2^{3-} + 4NH_3 + Cu(S_2O_3)_3^{5-} \quad (1)$$

$$4Cu(S_2O_3)_3^{5-} + 16NH_3 + O_2 + 2H_2O \rightarrow 4Cu(NH_3)_4^{2+} + 12S_2O_3^{2-} + 4OH^- \quad (2)$$

However, the major limitation of industrial application of thiosulfate leaching technique is the challenge in recovery of gold thiosulfate complex ($Au(S_2O_3)_2^{3-}$) from solution.

Various methods have been proposed to recover $Au(S_2O_3)_2^{3-}$, such as metal replacement and adsorption. However, replacing by metal caused great metal consumption and other metals co-precipitated problems, which was not economical (Guerra and Dreisinger, 1999). Adsorption by ion-exchange resin was also studied, while the easy pulverization of resin, high costs and hard elution of gold(I) limit its application (Xu et al., 2019). Activated carbon (AC), wildly used in gold cyanide leaching process to recover gold-cyanide complex from leaching solutions, is recognized as the promising adsorbent to adsorb $Au(S_2O_3)_2^{3-}$. However, $Au(S_2O_3)_2^{3-}$ is extremely hard to adsorb on AC (Gallagher et al., 1990). Other adsorbents such as modified AC, mesoporous silica, etc., also showed poor adsorption capacity to $Au(S_2O_3)_2^{3-}$ (Chen et al., 2020b, 2020c; Peng et al., 2018, 2019; Wang et al., 2020a).

Sulfur-rich molybdenum disulfide (MoS_2) exhibits strong interaction with Au(I) owing to hard and soft acids and bases fundamental principle (HSAB principle) and excellent photocatalytic reduction properties (Jia et al., 2017; Li et al., 2014; Pearson, 1968; Peng et al., 2020; Zeng et al., 2020). Our previous studies have revealed that molybdenum disulfide (MoS_2) nanosheets exhibited quite high recovery capacity to $Au(S_2O_3)_2^{3-}$ (up to ~651 mg/g in 100 mg/L $Au(S_2O_3)_2^{3-}$), which is almost 600 times to capacity of AC; most importantly, MoS_2 not only can efficiently recover $Au(S_2O_3)_2^{3-}$, but also reduce the $Au(S_2O_3)_2^{3-}$ to gold nanoparticles due to the excellent photocatalytic properties, which provided great potential to recover $Au(S_2O_3)_2^{3-}$ from solution, and in order to enhance the ability of reducing $Au(S_2O_3)_2^{3-}$, MoS_2/ZnS nano-

* Corresponding author at: Hubei Key Laboratory of Mineral Resources Processing and Environment, Wuhan University of Technology, Luoshi Road 122, Wuhan, Hubei 430070, China.
E-mail address: feifeijia@whut.edu.cn (F. Jia).

https://doi.org/10.1016/j.hydromet.2020.105514
Received 15 July 2020; Received in revised form 16 October 2020; Accepted 23 October 2020
Available online 27 October 2020

heterjunction was prepared, the reduction capacity of $Au(S_2O_3)_2^{3-}$ on MoS_2/ZnS nano-heterjunction reached to 1120.56 mg/g, the enhancement was attributed to the higher photogenerated electrons transfer efficiency of MoS_2/ZnS nano-heterjunction (Zhan et al., 2020b). Considering the difficulty of solid-liquid separation of nanomaterials, MoS_2 was anchored to Chitosan aerogel to form MoS_2/Chitosan aerogel (Chen et al., 2020a). The MoS_2/Chitosan aerogel solved the difficulty of solid-liquid separation of nanomaterials in somewhat, but the reduction capacity of $Au(S_2O_3)_2^{3-}$ on MoS_2/Chitosan aerogel decreased to 425.7 mg/g. Therefore, it's emergency to develop easily separated MoS_2-based materials with excellent $Au(S_2O_3)_2^{3-}$ reduction capacity.

To solve the above issue, one of effective approaches is to prepare magnetic MoS_2 composite. Fe_3O_4 is considered as a widely used magnetic materials in photocatalysis. Fe_3O_4 not only can achieve easy separation from liquids, but also can enhance the transformation of photoexcited electrons (Lin et al., 2018; Padhi et al., 2017). The conductivity of Fe_3O_4 reaches as high as 1.9×10^6 Sm^{-1}, which makes it possible for promoting the photogenerated electrons separation and transport rates, and effectively improving the photocatalytic performance (Gao et al., 2016).

Thus, in this study, the magnetic MoS_2@Fe_3O_4 shell-core composite was constructed. It was firstly proposed for reduction of $Au(S_2O_3)_2^{3-}$ on MoS_2@Fe_3O_4 composite. The structure, morphology and chemical properties of MoS_2@Fe_3O_4 composite were characterized by XRD, TEM, VSM and XPS. The in-situ reduction performances of $Au(S_2O_3)_2^{3-}$ on MoS_2@Fe_3O_4 composite were studied in aqueous solutions. Subsequently, the mechanism was investigated by photocurrent, EIS and UV–vis absorption spectra. The aim was to achieve highly efficiency recovering gold in gold thiosulfate technique.

2. Experimental

2.1. Chemicals

Hexaammonium heptamolybdate tetrahydrate ($(NH_4)_6Mo_7O_{24}\cdot 4H_2O$), thiourea ($CH_4N_2S$), anhydrous sodium acetate (CH_3COONa), ferric chloride hexahydrate ($FeCl_3\cdot 6H_2O$) and ethylene glycol ($C_2H_6O_2$) used in this experiment were of analytical grade and bought from Sinopharm Chemical Reagent Co., Ltd. (China). Ammonium thiosulfate ($(NH_4)_2S_2O_3$) was obtained from Aladdin Co. Ltd. (China). Standard gold chloroauric acid ($HAuCl_4$, 1000 mg/L) was purchased from Well Group Scientific Ltd. (USA). Deionized water (18.2 MΩ·cm) was produced by Milli-Q instrument (Millipore USA).

2.2. Fabrication of MoS_2@Fe_3O_4 shell-core composite

2.2.1. Preparation of Fe_3O_4 nanospheres

Fe_3O_4 nanospheres were synthesized by solvothermal method (Wang et al., 2019a). The process is as follows. Firstly, 1.35 g $FeCl_3\cdot 6H_2O$ and 3.60 g CH_3COONa were dissolved into 50 mL ethylene glycol to form homogeneous solution. Then, the solution was transferred into a 100 mL Teflon-lined stainless steel autoclave at 200 °C for 8 h. After cooling down to room temperature, the precipitate was washed with deionized water and ethanol for several times to remove the residual chemicals, followed by drying in vacuum oven at 60 °C.

2.2.2. Preparation of shell-core structured MoS_2@Fe_3O_4 composite

MoS_2@Fe_3O_4 shell-core composite was synthesized by hydrothermal process (Lin et al., 2015). 1 mmol $(NH_4)_6Mo_7O_{24}\cdot 4H_2O$ and 30 mmol CN_2H_4S were added into 40 mL deionized water and stirred to form homogeneous solution. Then, 80 mg Fe_3O_4 nanospheres was added into the above solution and followed by ultrasound to disperse using a Elmasonic P 30H ultrasonic processor (37 kHz and 150 W, Elma, Germany) for 10 min in a water bath. Subsequently, the solution was transferred into a 100 mL Teflon-lined stainless-steel autoclave at 180 °C for 24 h. After cooling down to room temperature, the black precipitate was washed with deionized water and ethanol followed by vacuum freeze-drying. The contents of Fe, Mo and S elements in MoS_2@Fe_3O_4 composite were detected by an inductively coupled plasma (ICP), and the results were listed in Table S1. It was found that the mole ratio of Mo: S was 1:1.97 and the mass ratio of Fe_3O_4 to MoS_2 was around 1: 5.05. For comparison, the pure MoS_2 nanosheets were prepared by the same procedure without the addition of Fe_3O_4 nanospheres.

2.3. Measurements

XRD patterns of MoS_2, Fe_3O_4 and MoS_2@Fe_3O_4 composite were obtained by an advance diffractometer (D8, Bruker, Germany). The TEM images were observed using a transmission electron microscope (TEM, JEM2100F, JEOL, Japan). The XPS spectra was obtained by X-ray photoelectron spectroscopy (ESCALAB 250Xi, Thermo Fisher Scientific Co. Ltd., USA). The Zeta potential of MoS_2@Fe_3O_4 composite was measured by a Malvern Zeta-sizer Nano ZS90. The magnetic hysteresis loops of Fe_3O_4 and MoS_2@Fe_3O_4 composite were obtained from a VSM (PPMS-9T, Quantum Design). UV–vis diffuse reflectance spectra were gained from an UV–vis–Nir spectrometer (Lambda 750S, PerkinElmer). Transient photocurrent responses and electrochemical impedance spectroscopy (EIS) of samples were tested on an electrochemical workstation (CHI650E) with conventional three-electrode system. A FTO glass coated with samples was as working electrode, a platinum electrode and a standard calomel electrode were served as counter electrode and reference electrode, respectively. Inductively coupled plasma-optical emission spectrum (ICP-OES, Prodigy, USA) was used for detecting the elements concentration in composite. Atomic absorption spectrophotometer (AAS, AA-6880 SHIMADZU, Japan) was used to obtain the initial and residual concentration of $Au(S_2O_3)_2^{3-}$ in the solution.

2.4. Reduction of $Au(S_2O_3)_2^{3-}$

Aqueous solution of $Au(S_2O_3)_2^{3-}$ was prepared by adding $HAuCl_4$ into $(NH_4)_2S_2O_3$ solution under pH of 10 with mole ratio of 1:4 according to the previous literature (Zeng et al., 2020; Zhan et al., 2020b). Reduction experiments of $Au(S_2O_3)_2^{3-}$ on prepared samples was carried out as follows. Firstly, 10 mg of samples (MoS_2, Fe_3O_4 or MoS_2@Fe_3O_4 composite) were added into 150 mL $Au(S_2O_3)_2^{3-}$ with desired concentration under pH of 10. And then, the suspension was stirred at 180 rpm at 25 °C under sunlight. At different interval time, 1–2 mL of suspension was sucked and filtered with 0.22 μm membrane. The $Au(S_2O_3)_2^{3-}$ concentration was determined by AAS. To study the effect of pH on $Au(S_2O_3)_2^{3-}$ reduction on MoS_2@Fe_3O_4 composite, the pH of $Au(S_2O_3)_2^{3-}$ solution was adjusted from 8 to 11.

$Au(S_2O_3)_2^{3-}$ reduction capacity was calculated by Eq. (3).

$$R = (C_0 - C_t) \times V/m \quad (3)$$

where R is the reduction capacity of $Au(S_2O_3)_2^{3-}$, C_0 and C_t (mg/L) are the concentrations of $Au(S_2O_3)_2^{3-}$ in the solution at the initial and t time, respectively. V (L) is the volume of $Au(S_2O_3)_2^{3-}$ solution and m (g) is the mass of used samples.

3. Results and discussion

3.1. Characterization of MoS_2@Fe_3O_4 composite

The phase of Fe_3O_4 nanosphere, pure MoS_2 and MoS_2@Fe_3O_4 composite were obtained by XRD. Fig. 1 shows the XRD patterns of Fe_3O_4 nanospheres, pure MoS_2 and MoS_2@Fe_3O_4 composite. As shown in Fig. 1, the diffraction peaks at 2-theta degree of 30.1°, 35.4°, 56.9° and 62.5° were corresponding to the (220), (311), (400), (511) and (440) planes of Fe_3O_4 according to JCPDS Card no.89–0691. For pure MoS_2 nanosheets, the diffraction peaks at 13.9°, 32.5°, 35.9° and 57.3° were

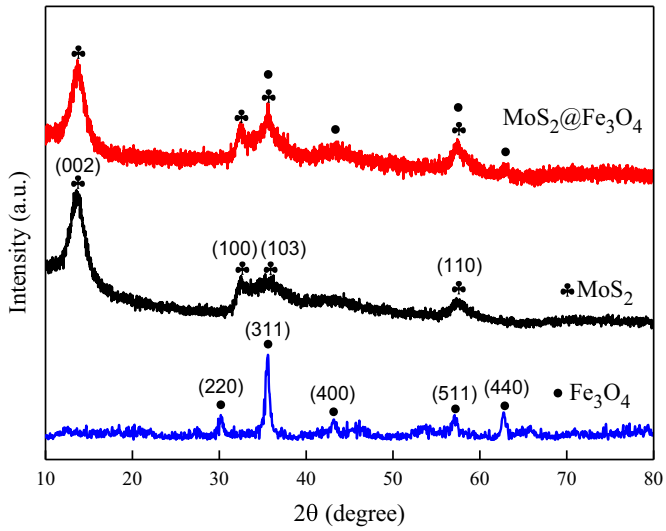

Fig. 1. XRD patterns of Fe_3O_4 nanospheres, pure MoS_2 and MoS_2@-Fe_3O_4 composite.

attributed to the (002), (100), (103) and (110) planes of MoS_2 according to the JCPDS Card no. 37–1492. After formation of the composite between MoS_2 and Fe_3O_4, the characteristic peaks of both MoS_2 and Fe_3O_4 were found, indicating the successful preparation of MoS_2@Fe_3O_4 composite.

Fig. 2 shows the magnetic hysteresis loops of Fe_3O_4 nanospheres and MoS_2@Fe_3O_4 composite. The saturated magnetization of Fe_3O_4 nanospheres reached 65.12 emu/g, indicating super magnetism of Fe_3O_4, after the "shell" of MoS_2 growing on the "core" of Fe_3O_4 nanospheres, the saturated magnetization decreased to 9.83 emu/g. The magnetic "shell-core" MoS_2@Fe_3O_4 composite was prone to be separated from the liquids by Magnet, as shown in the insert photograph.

The morphologies of Fe_3O_4 nanospheres, MoS_2 nanosheets and MoS_2@Fe_3O_4 composite are illustrated in Fig. 3. Clearly, the as-prepared Fe_3O_4 was typically nanospheres (Fig. 3(a–b)). Fig. 3(c–d) displayed the TEM images of pure MoS_2 nanosheets, it can be seen that MoS_2 nanosheets stacked with each other, which decreased the specific surface area. Reported that the active sites of MoS_2 usually appeared at the "edge" of MoS_2, and the basal plane was less active, thus, the stack of MoS_2 nanosheets lead to poor properties in catalysis, adsorption, etc.

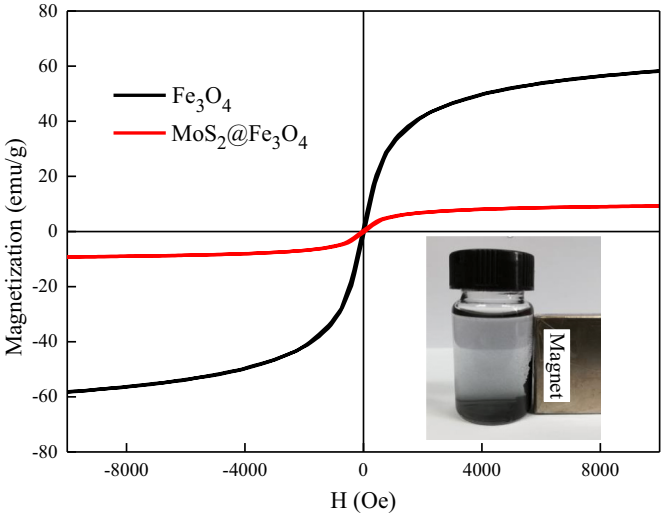

Fig. 2. Magnetic hysteresis loop of Fe_3O_4 nanospheres and MoS_2@-Fe_3O_4 composite.

(Chang et al., 2021; Wang et al., 2019b; Yuan et al., 2019, 2020; Zhan et al., 2020a). Fig. 3(e–f) illustrates the TEM images of MoS_2@Fe_3O_4 composite. In-situ growing the MoS_2 nanosheets on Fe_3O_4 nanospheres, the hierarchical shell-core structured MoS_2@Fe_3O_4 composite was obtained, as expected, the MoS_2 decorated on Fe_3O_4 to form the "shell", which reduced the stacks of MoS_2 nanosheets and exposed more active sites. What's more, the magnetic "core" Fe_3O_4 could realize easy separation from solutions.

3.2. *In-situ reduction of* $Au(S_2O_3)_2^{3-}$

The catalytic reduction activities of $Au(S_2O_3)_2^{3-}$ on MoS_2@Fe_3O_4 composite were carried out under natural light irradiation. The reduction performances of Fe_3O_4, MoS_2 nanosheets and MoS_2@Fe_3O_4 composite (initial $Au(S_2O_3)_2^{3-}$ concentration ~103 mg/L, pH 10) were illustrated in Fig. 4(a). It could be seen that Fe_3O_4 nanospheres had low reduction capacity of $Au(S_2O_3)_2^{3-}$, while for pure MoS_2 and MoS_2@-Fe_3O_4 composite, the reduction capacity of $Au(S_2O_3)_2^{3-}$ was extremely high, especially for MoS_2@Fe_3O_4 composite, the reduction capacity reached a maximum 1541.1 mg/g. It indicated that the efficient reduction of $Au(S_2O_3)_2^{3-}$ was mainly due to the properties of MoS_2, which was consistent with our previous study. Meanwhile, it was obvious that the reduction rate of $Au(S_2O_3)_2^{3-}$ on MoS_2@Fe_3O_4 composite was much faster than pure MoS_2 nanosheets, which could be attributed to the special "shell-core" structure of MoS_2@Fe_3O_4 composite that exposed to more "edges" active sites.

Fig. 4(b) shows the effect of initial concentration of $Au(S_2O_3)_2^{3-}$ on gold reduction on MoS_2@Fe_3O_4 composite. It can be seen that the reduction capacity of $Au(S_2O_3)_2^{3-}$ on MoS_2@Fe_3O_4 composite was significant prompted with the $Au(S_2O_3)_2^{3-}$ initial concentration increasing and exceed 2000 mg/g at the concentration of 180.1 mg/L, which indicating MoS_2@Fe_3O_4 composite was an excellent material to recover $Au(S_2O_3)_2^{3-}$ from liquids.

Fig. 4(c) depicts the effect of pH on reduction of $Au(S_2O_3)_2^{3-}$ on MoS_2@Fe_3O_4 composite. The pH ranging 8 to 11 was investigated because the thiosulfate leaching usually happen in this pH range. The reduction capacity boosted with increasing pH to 10 and then gradually decreased. Zeta potential of materials are usually important to series of reactions happened in liquid. Fig. 4(d) illustrates the zeta potential of MoS_2@Fe_3O_4 composite at the pH range of 7 to 12. It could be seen that the zeta potential of MoS_2@Fe_3O_4 composite was below −35 mV in the overall pH range, indicating the electrostatic interaction between MoS_2@Fe_3O_4 composite and anion $Au(S_2O_3)_2^{3-}$ was unable to occur. The reduction mechanism of $Au(S_2O_3)_2^{3-}$ was explained in detail below.

To further verify the in-situ reduction of $Au(S_2O_3)_2^{3-}$ on MoS_2@-Fe_3O_4 composite, XRD, XPS and TEM were used to explore the MoS_2@Fe_3O_4 composite. Fig. 5 shows the results of XRD and XPS. The XRD patterns (Fig. 5(a)) of MoS_2@Fe_3O_4 composite after $Au(S_2O_3)_2^{3-}$ reduction exhibited four new peaks locating at the 2-theta of 38.2°, 44.4°, 64.7° and 77.6°, which were assigned to Au^0, indicating Au(I) in $Au(S_2O_3)_2^{3-}$ was reduced to Au^0 on MoS_2@Fe_3O_4 composite (Zeng et al., 2020). Fig. 5(b) illustrates the high resolution spectrum of Au 4f, two peaks at 84.48 eV and 88.13 eV were related to the Au $4f_{7/2}$ and Au $4f_{5/2}$ of Au^0. TEM images are applied to further confirm the reduction of Au $(S_2O_3)_2^{3-}$ (Fig. 6). Clearly, many nanoparticles loaded on MoS_2@Fe_3O_4 composite, indicating the Au(I) was reduced to gold nanoparticles.

The surface chemical composition of MoS_2@Fe_3O_4 composite before and after $Au(S_2O_3)_2^{3-}$ reduction was investigated by XPS. The high resolution of Mo 3d and S 2p spectra before and after $Au(S_2O_3)_2^{3-}$ reduction were showed in Fig.S1. In Mo 3d spectrum before $Au(S_2O_3)_2^{3-}$ reduction (Fig.S1(a)), the peaks at 229.38 eV and 232.58 eV represented the Mo (IV) in MoS_2; binding energies at 230.48 eV and 233.98 eV related to the Mo(V); the peak at 235.98 eV was ascribed to the Mo(VI); the binding energy of 226.48 eV was corresponding to the S^{2-} in MoS_2 (Addou et al., 2015; Wang et al., 2020b). In S 2p spectrum before $Au(S_2O_3)_2^{3-}$ reduction (Fig.S1(c)), the peaks at 162.28 eV and 163.48 eV were ascribed to

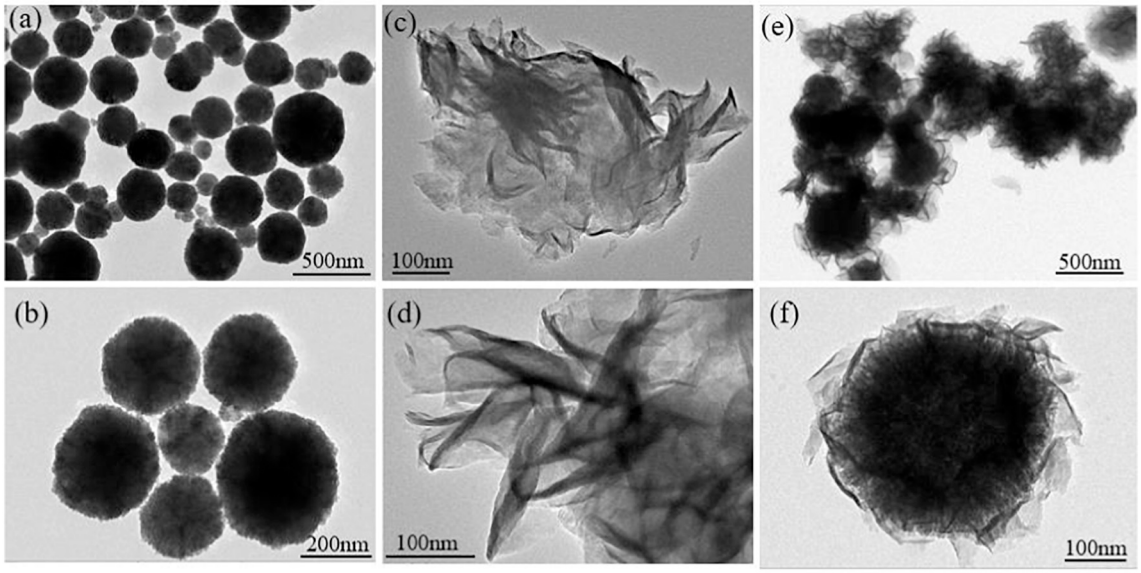

Fig. 3. TEM images of Fe_3O_4 nanospheres (a–b), pure MoS_2 (c–d) and MoS_2@Fe_3O_4 composite (e–f).

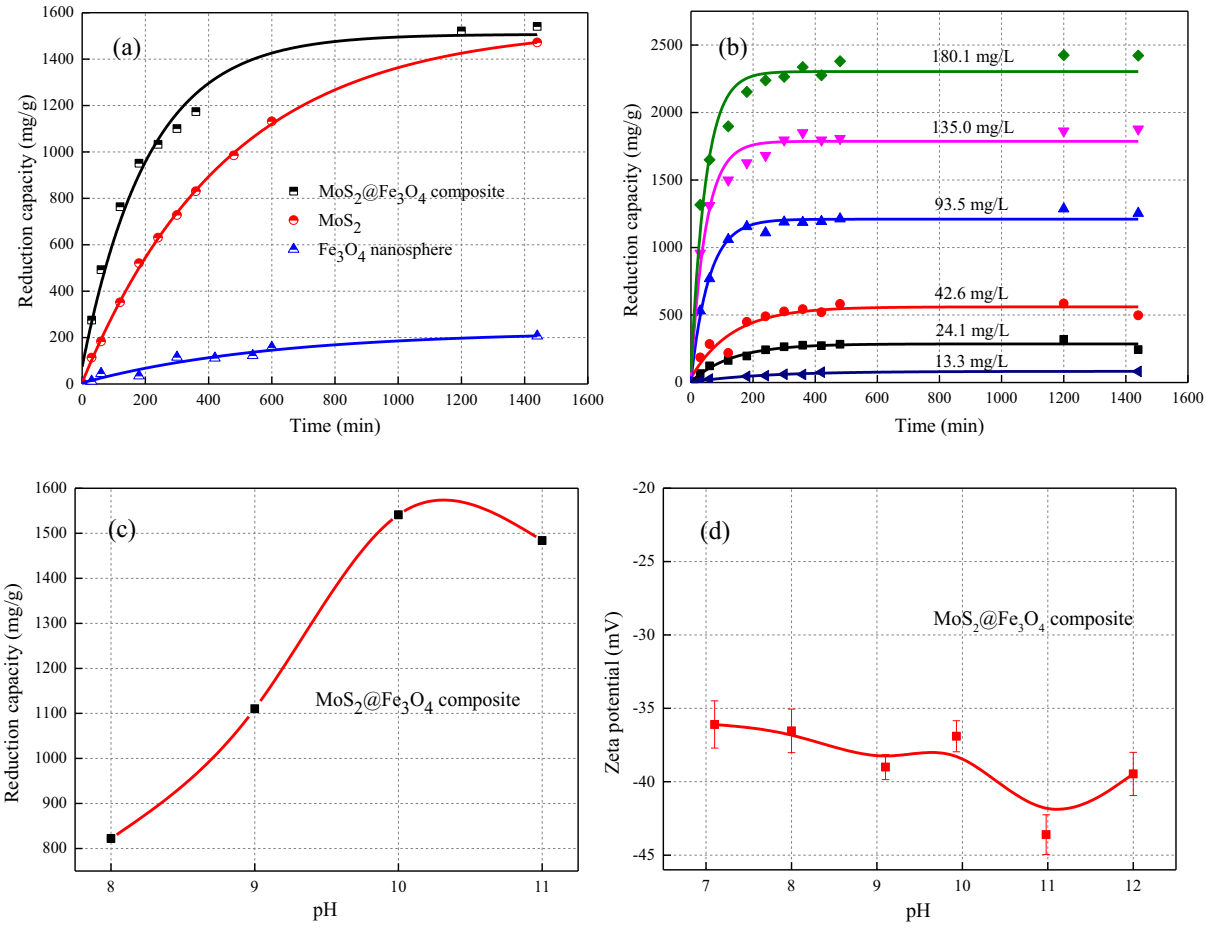

Fig. 4. Reduction performance of $Au(S_2O_3)_2^{3-}$ on Fe_3O_4, MoS_2 and MoS_2@Fe_3O_4 composite (a), effect of initial concentration of $Au(S_2O_3)_2^{3-}$ (b), effect of pH (c) and zeta potential of MoS_2@Fe_3O_4 composite (d).

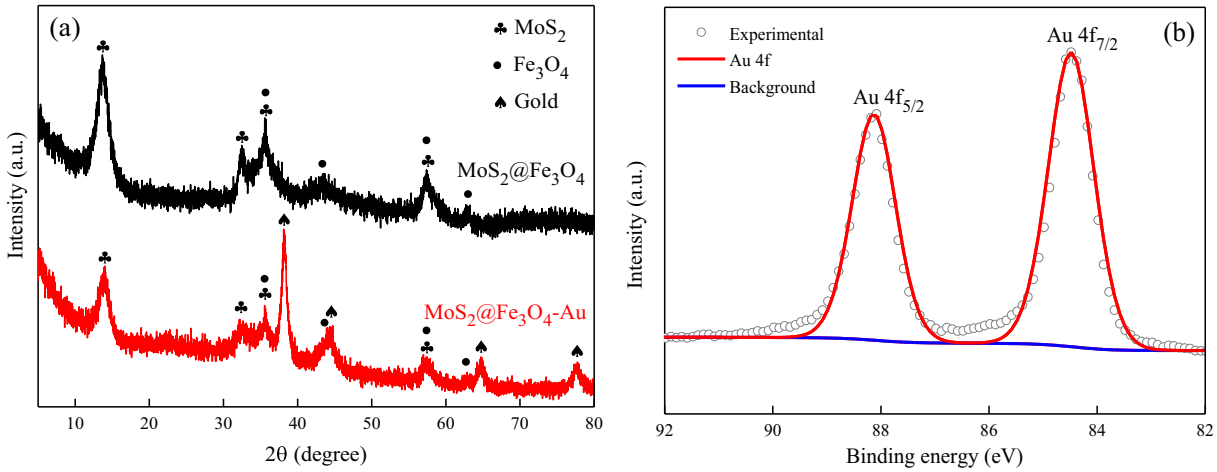

Fig. 5. XRD patterns (a) and Au 4f XPS spectrum (b) of MoS_2@Fe_3O_4 composite after $Au(S_2O_3)_2^{3-}$ reduction.

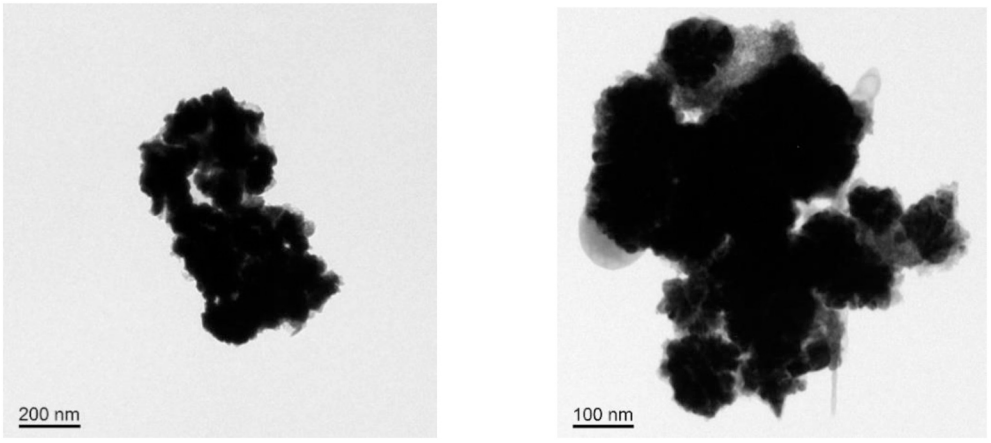

Fig. 6. TEM images of MoS_2@Fe_3O_4 composite after $Au(S_2O_3)_2^{3-}$ reduction.

the S^{2-} in MoS_2; the peak observed at 164.78 eV was ascribed to the defects in MoS_2 (Lin et al., 2017; Sun et al., 2020). After the reduction of $Au(S_2O_3)_2^{3-}$ on MoS_2@Fe_3O_4 composite (Fig.S1(b) and (d)), the chemical composition of MoS_2 did not change indicating MoS_2 was quite stable during reduction of $Au(S_2O_3)_2^{3-}$.

3.3. Origin of $Au(S_2O_3)_2^{3-}$ reduction on MoS_2@Fe_3O_4 composite

The in-situ reduction of $Au(S_2O_3)_2^{3-}$ is original from the photocatalytic properties of MoS_2, thus, the photo-electrochemical properties of as-synthesized samples were investigated. Photocurrent response (Fig. 7(a)) were used to explore the separation efficiency of photo electrons and holes. It can be seen that MoS_2@Fe_3O_4 composite showed the greatest photocurrent intensity among pure MoS_2, Fe_3O_4 and MoS_2@Fe_3O_4 composite, which can be ascribed to that the combination of MoS_2 and Fe_3O_4 to enhance the separation of charges. The greatest photocurrent intensity of MoS_2@Fe_3O_4 composite indicated that MoS_2@Fe_3O_4 composite would have most photogenerated charges for photocatalytic reduction, therefore, MoS_2@Fe_3O_4 composite have the greatest Au(I) reduction capacity. It also found that MoS_2 and Fe_3O_4 had photocurrent response, indicating the two materials also produced photogenerated electrons to reduce Au(I), meanwhile, the Fe_3O_4 had higher photocurrent than pure MoS_2, whereas the Au(I) reduction capacity was much worse than pure MoS_2 from the experimental data, which was because sulfur-containing MoS_2 was beneficial for adsorption of $Au(S_2O_3)_2^{3-}$ from solution due to strong soft-soft interaction between S atoms and precious metal, furtherly, the photoelectrons of MoS_2 could transfer to $Au(S_2O_3)_2^{3-}$ better.

EIS was used to investigate the charge-transfer resistance, the smaller semicircle represented smaller charge-transfer resistance (Peng et al., 2017). The EIS Nyquist plots exhibited that MoS_2@Fe_3O_4 composite owned smaller semicircle than pure MoS_2, revealing the shell-core structured composite reduced the charge-transfer resistance, and was beneficial to transfer photoelectrons to Au(I). Therefore, the MoS_2@-Fe_3O_4 composite displayed higher and faster $Au(S_2O_3)_2^{3-}$ reduction than pure MoS_2. What's more, Fe_3O_4 nanospheres exhibited small charge-transfer resistance, which was ascribe to the excellent conductivity of Fe_3O_4, whereas its poor reduction capacity of $Au(S_2O_3)_2^{3-}$ was due to the poor affinity between Fe_3O_4 nanospheres and $Au(S_2O_3)_2^{3-}$.

The light-absorbed properties of MoS_2, Fe_3O_4 and MoS_2@Fe_3O_4 composite were investigated by UV–vis adsorption spectrum, as illustrated in Fig. 7(c). It can be seen that MoS_2 and MoS_2@Fe_3O_4 composite showed excellent absorption both in ultraviolet and visible light regions, whereas the Fe_3O_4 showed absorption only in ultraviolet and little part of visible regions, which indicating MoS_2-based photocatalysts can utilize visible-light efficiently.

The energy gap (E_g), conduction band energy (E_{CB}) and valence band energy (E_{VB}) is important to photocatalytic reactions. The energy gap can be calculated according to the following equation (Zhao et al., 2016):

$$(\alpha h\nu)^n = A(h\nu - E_g) \quad (4)$$

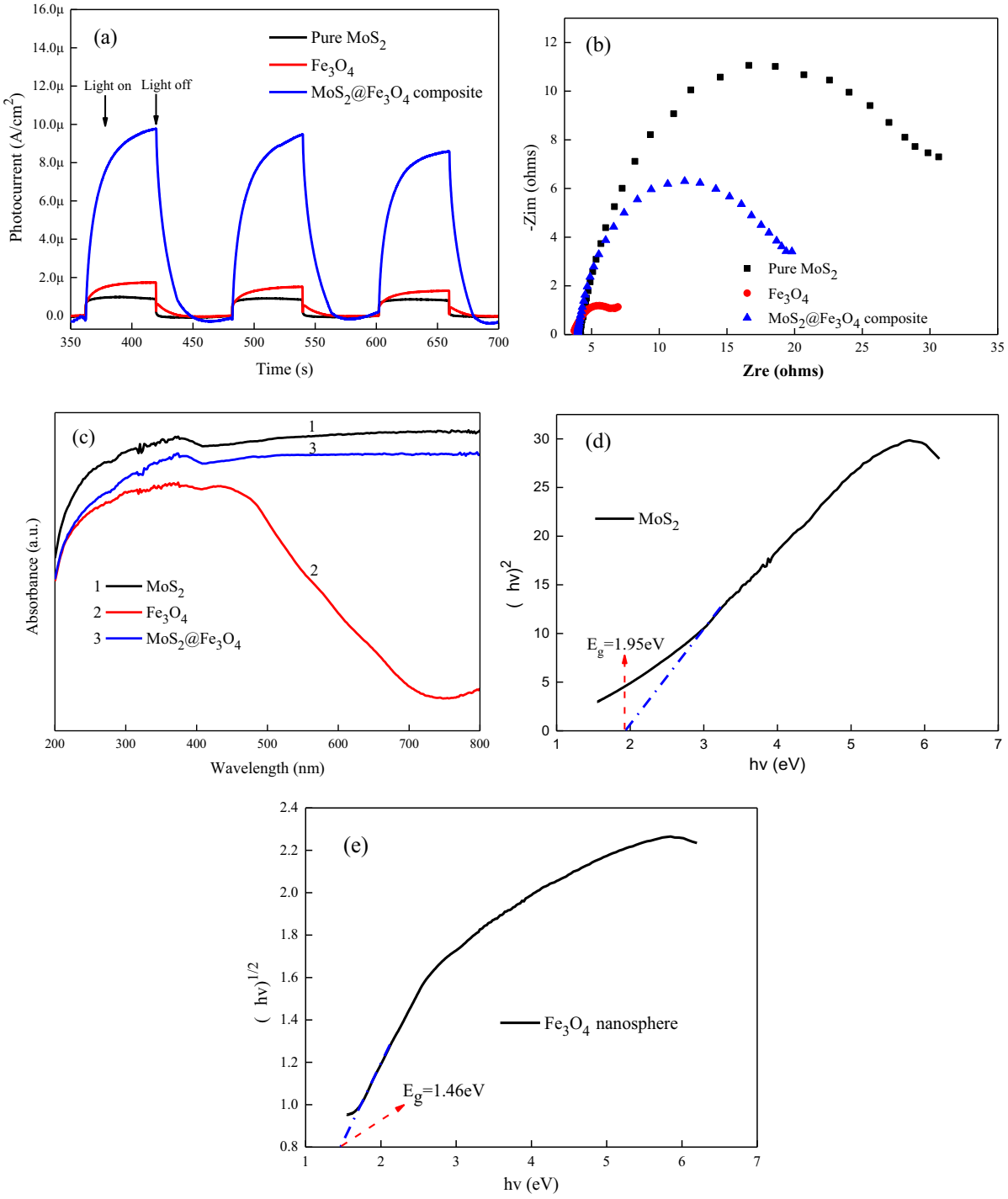

Fig. 7. Photocurrent responses (a), EIS curve (b), UV–vis absorption spectra (c) and the Kubelka-Munk transformed reflectance plot of MoS_2 (d) and Fe_3O_4 (e).

where α, h, v and A are absorption coefficient, Planck's constant, light frequency and a constant, respectively. The n depends on the type of semiconductor, n is 2 for MoS_2 and n is 1/2 for Fe_3O_4 in this work (Vinodhkumar et al., 2020; Zong et al., 2008). The energy gap can be estimated by extrapolating the linear portion of the $(\alpha hv)^n$ versus hv curve (Kubelka-Munk transformed reflectance plot), as shown in Fig. 7 (d–e). The Eg was 1.95 eV for MoS_2 and 1.46 eV for Fe_3O_4. Furthermore, The E_{CB} and E_{VB} can be calculated by the following equations (Xu et al., 2008):

$$E_{CB} = X - E^e - 0.5E_g \quad (5)$$

$$E_{VB} = E_g + E_{CB} \quad (6)$$

where X is the absolute electronegativity of semiconductor, E^e is the energy of free electrons on the hydrogen scale (4.5 eV). According the above equations, the E_{CB} and E_{VB} values of MoS_2 were − 0.155 eV and 1.795 eV, the E_{CB} and E_{VB} values of Fe_3O_4 were − 0.9 eV and 0.56 eV.

Based on these results, the mechanism of reduction of $Au(S_2O_3)_2^{3-}$ by MoS_2@Fe_3O_4 composite as photocatalyst was proposed and illustrated in Fig. 8. Under visible light irradiation, MoS_2@Fe_3O_4 composite produced rich photogenerated electrons, and the photoelectrons on conduction band (CB) of Fe_3O_4 could easily transfer to the CB of MoS_2 due to

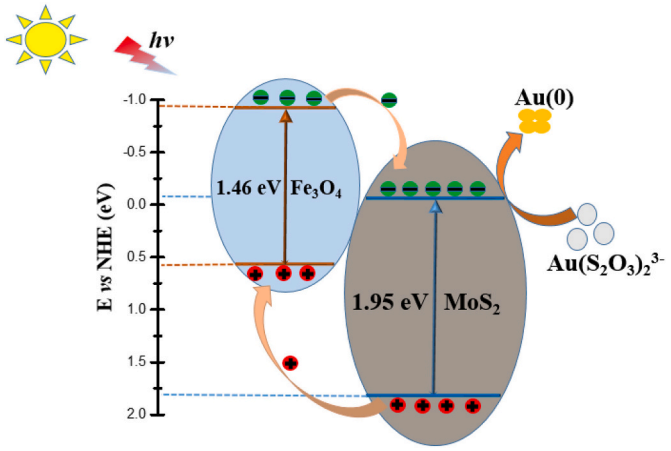

Fig. 8. Mechanism of photocatalytic reduction of $Au(S_2O_3)_2^{3-}$ on MoS_2@-Fe_3O_4 composite.

more negative CB value of Fe_3O_4. Meanwhile, the holes on valence band (VB) of MoS_2 could be injected to VB of Fe_3O_4. The combination rate of photoelectrons/holes was greatly decreased, more effective photoelectrons gathered on MoS_2. Thanks to the strong interaction (HSAB) between gold and sulfur atoms, $Au(S_2O_3)_2^{3-}$ was prone to be adsorbed on MoS_2, and the photoelectrons made the $Au(S_2O_3)_2^{3-}$ reduce to Au^0 directly, which resulted in the in-situ reduction of $Au(S_2O_3)_2^{3-}$ on MoS_2@Fe_3O_4 composite. The possible reactions were listed as follows:

$$MoS_2@Fe_3O_4 + hv \rightarrow e^- + h^+ \quad (7)$$

$$Au^+ + e^- \rightarrow Au^0 \quad (8)$$

4. Conclusion

In summary, shell-core structured MoS_2@Fe_3O_4 composite was synthesized by a simple hydrothermal route and realized in-situ reducing $Au(S_2O_3)_2^{3-}$ to Au^0 with remarkable reduction capacity. The excellent reduction performance was ascribed to more efficient transfer and less recombination of photoexcited electrons-holes pairs. More importantly, the magnetic properties of MoS_2@Fe_3O_4 composite achieved easy separation from solutions. MoS_2@Fe_3O_4 composite was proved to be a promising material for efficient recovery of gold from solutions.

Author statement

I am hereby to state that the manuscript mentioned above contains original work and has not been published or is not being considered for publication elsewhere. Also, all of the authors of the manuscript have agreed for this submission and author contributions are as listed.

CRediT authorship contribution statement

Kaige Sun: Conceptualization, Methodology, Investigation, Formal analysis, Writing - original draft. **Shangjian Mao:** Investigation, Formal analysis. **Weiquan Zhan:** Methodology, Formal analysis. **Chang Liu:** Formal analysis. **Feifei Jia:** Conceptualization, Resources, Writing - review & editing, Supervision, Funding acquisition. **Shaoxian Song:** Resources, Supervision, Writing - review & editing.

Declaration of Competing Interest

The authors declare that they have no known competing financial interests or personal relationships that could have appeared to influence the work reported in this paper.

Acknowledgements

This work was supported by the National Natural Science Foundation of China (No. 51974216, 51704212 and 51704220), the Natural Science Foundation of Hubei Province (No. 2019CFB536).

Appendix A. Supplementary data

Supplementary data to this article can be found online at https://doi.org/10.1016/j.hydromet.2020.105514.

References

Addou, R., McDonnell, S., Barrera, D., Guo, Z., Azcatl, A., Wang, J., Zhu, H., Hinkle, C.L., Quevedo-Lopez, M., Alshareef, H.N., 2015. Impurities and electronic property variations of natural MoS_2 crystal surfaces. ACS Nnao 9, 9124–9133.
Chang, L.P., Cao, Y.J., Peng, W.J., Li, C., Fan, G.X., Song, X.Y., Jia, C.X., 2021. Insight into the effect of oxidation degree of graphene oxides on their removal from wastewater via froth flotation. Chemosphere 262, 127837.
Chen, P., Liang, Y.M., Yang, B.Q., Jia, F.F., Song, S.X., 2020a. In situ reduction of Au(I) for efficient recovery of gold from thiosulfate solution by the 3D MoS_2/chitosan aerogel. ACS Sustain. Chem. Eng. 8, 3673–3680.
Chen, S.L., Zi, F.T., Hu, X.Z., Chen, Y.L., Yang, P., Wang, Q., Qin, X.C., Cheng, H.L., Liu, Y., He, Y., 2020b. Interfacial properties of mercaptopropyl-functionalised silica gel and its adsorption performance in the recovery of gold (I) thiosulfate complex. Chem. Eng. J. 393, 124547.
Chen, Y.L., Zi, F.T., Hu, X.Z., Yang, P., Ma, Y.P., Cheng, H.L., Wang, Q., Qin, X.C., Liu, Y., Chen, S.L., 2020c. The use of new modified activated carbon in thiosulfate solution: a green gold recovery technology. Sep. Purif. Technol. 230, 115834.
Gallagher, N.P., Hendrix, J.L., Milosavljevic, E.B., Nelson, J.H., Solujic, L., 1990. Affinity of activated carbon towards some gold(I) complexes. Hydrometallurgy 25 (3), 305–316.
Gao, N.L., Lu, Z.Y., Zhao, X.X., Zhu, Z., Wang, Y.S., Wang, D.D., Hua, Z.F., Li, C.X., Huo, P.W., Song, M.S., 2016. Enhanced photocatalytic activity of a double conductive C/Fe3O4/Bi2O3 composite photocatalyst based on biomass. Chem. Eng. J. 304, 351–361.
Guerra, E., Dreisinger, D., 1999. A study of the factors affecting copper cementation of gold from ammoniacal thiosulphate solution. Hydrometallurgy 51 (2), 155–172.
Jia, F.F., Wang, Q.M., Wu, J.S., Li, Y.M., Song, S.X., 2017. Two-dimensional molybdenum disulfide as a superb adsorbent for removing Hg^{2+} from water. ACS Sustain. Chem. Eng. 5, 7410–7419.
Li, Y.C., Tian, H.Y., Xiao, C.S., Ding, J.X., Chen, X.S., 2014. Efficient recovery of precious metal based on Au–S bond and electrostatic interaction. Green Chem. 16, 4875–4878.
Lin, T.R., Wang, J., Guo, L.Q., Fu, F.F., 2015. Fe_3O_4@MoS_2 core-shell composites: preparation, characterization, and catalytic application. J. Phys. Chem. C 119, 13658–13664.
Lin, L.X., Miao, N.H., Huang, J.T., Zhang, S.W., Zhu, Y.Q., Horsell, D.D., Ghosez, P., Sun, Z.M., Allwood, D.A., 2017. A photocatalyst of sulphur depleted monolayered molybdenum sulfide nanocrystals for dye degradation and hydrogen evolution reaction. Nano Energy 38, 544–552.
Lin, X.Z., Wang, X., Zhou, Q.W., Wen, C.Y., Su, S.Q., Xiang, J., Cheng, P.F., Hu, X.B., Li, Y., Wang, X., Gao, X.S., Nozel, R., Zhou, G.Z., Zhang, Z., Liu, J.M., 2018. Magnetically recyclable MoS_2/Fe_3O_4 hybrid composite as visible light responsive photocatalyst with enhanced photocatalytic performance. ACS Sustain. Chem. Eng. 7, 1673–1682.
Liu, X.L., Jiang, T., Xu, B., Zhang, Y., Li, Q., Yang, Y.B., He, Y.H., 2020. Thiosulphate leaching of gold in the Cu-NH_3-$S_2O_3^{2-}$-H_2O system: an updated thermodynamic analysis using predominance area and species distribution diagrams. Miner. Eng. 151, 106336.
Muir, D.M., Aylmore, M.G., 2004. Thiosulphate as an alternative to cyanide for gold processing-issues and impediments. Miner. Process. Ext. Metall. 113, 2–12.
Padhi, D.K., Panigrahi, T.K., Parida, K., Singh, S.K., Mishra, P.M., 2017. Green synthesis of Fe_3O_4/RGO nanocomposite with enhanced photocatalytic performance for Cr (VI) reduction, phenol degradation, and antibacterial activity. ACS Sustain. Chem. Eng. 5, 10551–10562.
Pearson, R.G., 1968. Hard and soft acids and bases, HSAB, part 1: fundamental principles. J. Chem. Educ. 45, 581.
Peng, W.J., Li, H.Q., Song, S.X., 2017. Synthesis of fluorinated graphene/CoAl-layered double hydroxide composites as electrode materials for supercapacitors. ACS Appl. Mater. Interfaces 9 (6), 5204–5212.
Peng, W.J., Han, G.H., Cao, Y.J., Sun, K.G., Song, S.X., 2018. Efficiently removing Pb(II) from wastewater by graphene oxide using foam flotation. Colloid. Surf. A 556, 266–272.
Peng, W.J., Chang, L.P., Li, P.Y., Han, G.H., Huang, Y.K., Cao, Y.J., 2019. An overview on the surfactants used in ion flotation. J. Mol. Liq. 286, 110955.
Peng, W.J., Wang, W., Han, G.H., Huang, Y.K., Zhang, Y.S., 2020. Fabrication of 3D flower-like MoS_2/graphene composite as high-performance electrode for capacitive deionization. Desalination 473, 114191.
Sun, K.G., Peng, W.J., Li, H.Q., Song, S.X., 2018a. Recovery of $Au(CN)_2^-$ with magnetic reduced graphene oxide hydrogel in aqueous leach solution. Hydrometallurgy 176, 208–215.

Sun, K.G., Peng, W.J., Zhang, T.Y., Song, S.X., 2018b. Recovery of $Au(CN)_2^-$ by adsorption using reduced graphene oxide/ascorbic acid hydrogel. Miner. Process. Ext. Metall. 127, 140–145.

Sun, K.G., Jia, F.F., Yang, B.Q., Lin, C.S., Li, X.H., Song, S.X., 2020. Synergistic effect in the reduction of Cr (VI) with Ag-MoS_2 as photocatalyst. Appl. Mater. Today 18, 100453.

Vinodhkumar, G., Wilson, J., Inbanathan, S.S.R., Potheher, I.V., Ashokkumar, M., Peter, A.C., 2020. Solvothermal synthesis of magnetically separable reduced graphene oxide/Fe_3O_4 hybrid nanocomposites with enhanced photocatalytic properties. Physica B 580, 411752.

Wang, Q.M., Peng, L., Gong, Y.Y., Jia, F.F., Song, S.X., Li, Y.M., 2019a. Mussel-inspired Fe_3O_4@ Polydopamine (PDA)-MoS_2 core-shell nanosphere as a promising adsorbent for removal of Pb^{2+} from water. J. Mol. Liq. 282, 598–605.

Wang, W.C., Zhu, S., Cao, Y.N., Tao, Y., Li, X., Pan, D.L., Phillips, D.L., Zhang, D.Q., Chen, M., Li, G.S., Li, H.X., 2019b. Edge-enriched ultrathin MoS_2 embedded yolk-shell TiO_2 with boosted charge transfer for superior photocatalytic H_2 evolution. Adv. Funct. Mater. 29 (36), 1901958.

Wang, C.W., Chen, S.L., Chen, Y.L., Zi, F.T., Hu, X.Z., Qin, X.C., Zhang, Y., Yang, P., He, Y., He, P.Q., Lin, Y., Zhang, G.F., 2020a. Modification of activated carbon by chemical vapour deposition through thermal decomposition of thiourea for enhanced adsorption of gold thiosulfate complex. Sep. Purif. Technol. 241, 116632.

Wang, Q.M., Jia, F.F., Huang, A.H., Qin, Y., Song, S.X., Li, Y.M., Arroyo, M.A.C., 2020b. MoS_2@ sponge with double layer structure for high-efficiency solar desalination. Desalination 481, 114359.

Xu, H., Li, H.M., Wu, C.D., Chu, J.Y., Yan, Y.S., Shu, H.M., Gu, Z., 2008. Preparation, characterization and photocatalytic properties of Cu-loaded $BiVO_4$. J. Hazard. Mater. 153 (1–2), 877–884.

Xu, B., Li, K., Li, Q., Yang, Y.B., Liu, X.L., Jiang, T., 2019. Kinetic studies of gold leaching from a gold concentrate calcine by thiosulfate with cobalt-ammonia catalysis and gold recovery by resin adsorption from its pregnant solution. Sep. Purif. Technol. 213, 368–377.

Yuan, Y., Yang, B.Q., Jia, F.F., Song, S.X., 2019. Reduction mechanism of Au metal ions into Au nanoparticles on molybdenum disulfide. Nanoscale 11 (19), 9488–9497.

Yuan, Y., Zhan, W.Q., Jia, F.F., Song, S.X., 2020. Multi-edged molybdenite achieved by thermal modification for enhancing Pb(II) adsorption in aqueous solutions. Chemospere 251, 126369.

Zeng, S.L., Jia, F.F., Yang, B.Q., Song, S.X., 2020. In-situ reduction of gold thiosulfate complex on molybdenum disulfide nanosheets for a highly-efficient recovery of gold from thiosulfate solutions. Hydrometallurgy 195, 105369.

Zhan, W.Q., Jia, F.F., Yuan, Y., Liu, C., Sun, K.G., Yang, B.Q., Song, S.X., 2020a. Controllable incorporation of oxygen in MoS_2 for efficient adsorption of Hg^{2+} in aqueous solutions. J. Hazard. Mater. 384, 121382.

Zhan, W.Q., Yuan, Y., Yang, B.Q., Jia, F.F., Song, S.X., 2020b. Construction of MoS_2 nano-heterojunction via ZnS doping for enhancing in-situ photocatalytic reduction of gold thiosulfate complex. Chem. Eng. J. 394, 124866.

Zhao, W., Liu, Y., Wei, Z.B., Yang, S.G., He, H., Sun, C., 2016. Fabrication of a novel p-n heterojunction photocatalyst n-$BiVO_4$@ p-MoS_2 with core-shell structure and its excellent visible-light photocatalytic reduction and oxidation activities. Appl. Catal. B Environ. 185, 242–252.

Zong, X., Yan, H.J., Wu, G.P., Ma, G.J., Wen, F.Y., Wang, L., Li, C., 2008. Enhancement of photocatalytic H_2 evolution on CdS by loading MoS_2 as cocatalyst under visible light irradiation. J. Am. Chem. Soc. 130, 7176–7177.